A Discontinuous Galerkin Model for the Simulation of Chemotaxis Processes

Application to Stem Cell Injection After a Myocardial Infarction: Discontinuous Galerkin methods

Vermolen, F.J.; Crapts, L.Y.D.; Ryan, J.K.

DOI
10.1016/B978-0-12-811718-7.00006-X

Publication date
2018

Document Version
Final published version

Published in
Numerical Methods and Advanced Simulation in Biomechanics and Biological Processes

Citation (APA)
Vermolen, F. J., Crapts, L. Y. D., & Ryan, J. K. (2018). A Discontinuous Galerkin Model for the Simulation of Chemotaxis Processes: Application to Stem Cell Injection After a Myocardial Infarction: Discontinuous Galerkin methods. In M. Cerrolaza, S. Shefelbine, & D. Garzón-Alvarado (Eds.), *Numerical Methods and Advanced Simulation in Biomechanics and Biological Processes* (pp. 95-115). Elsevier. https://doi.org/10.1016/B978-0-12-811718-7.00006-X

Chapter 6

A Discontinuous Galerkin Model for the Simulation of Chemotaxis Processes: Application to Stem Cell Injection After a Myocardial Infarction

Discontinuous Galerkin Methods

F.J. Vermolen[1], L.Y.D. Crapts[1] and J.K. Ryan[2]
[1]*Delft University of Technology, Delft, The Netherlands;* [2]*University of East Anglia, Norwich, United Kingdom*

6.1 INTRODUCTION

In many biological processes, cells migrate in the direction to the gradient of a concentration. This process is commonly referred to as chemotaxis or haptotaxis in fluidic or solid environments, respectively. Chemotaxis of cells occurs not only in many important biological processes, such as wound healing, but also in tumor growth and metastasis. Healing processes typically involve the repair of tissues and, to this end, it is necessary that certain cells migrate and regenerate the appropriate tissues such as bone or skin. Cells secrete signaling agents by which either cells of the same or different phenotypes are attracted toward them so that certain biological processes such as the repair of extracellular matrix can occur. Furthermore, the immune response system operates on the basis of chemotactic migration of white blood cells toward pathogens as a result of biotic lactates that are effectively transported away from pathogens as a result of the acidification of the environment. In various treatments, it is aimed at trying to make certain cells migrate to desired locations. In this chapter, we consider the application of stem cell therapy to improve the structure and efficacy of the heart muscle, where stem cells activate migration of endothelial cells to damaged regions of the heart. An experimental study on stem cell migration induced by chemokines was presented in, among many other studies, Baek et al. (2011).

Myocardial infarctions have been a very common cause of death in the industrialized countries for many decades. The cause of a myocardial infarction (heart attack) gradually develops as a result of the increasing blockage of the coronal artery of the heart. This gradual blockage is referred to as atherosclerosis, see Shimamoto (1969) for an early experimental study. Once the coronal artery is blocked, then the flow of blood stops and herewith the transport of oxygen ceases, and then sudden death of heart tissue sets in. This is the myocardial infarction (heart attack). After a myocardial infarction, the mechanical structure of the heart tissue changes as a result of fibrosis (stiffening as a result of the development of fibrous tissue). An experimental reference regarding the temporal evolution of mechanical properties (in particular stiffening) of the scar tissue that develops after a myocardial infarction is given in Fomovsky and Holmes (2010), where they also observed that the collagen orientation tends to be more isotropically aligned in rats than in other animals such as pigs and goats. The dead part of the heart muscle no longer contracts and has become stiffer and thereby the pumping mechanism is inhibited, whereas the parts of the heart that are still viable are working harder. This causes rhythmic disorder and eventually heart failure and hence possibly sudden death of the patient.

Heart cells (cardiocytes) were thought to be irreplaceable (see for instance Olivetti et al., 1991); however, the more recent insights point at a "self-healing" capacity of the heart (see for instance Kajstura et al., 2008). Here it can be seen that

Numerical Methods and Advanced Simulation in Biomechanics and Biological Processes. https://doi.org/10.1016/B978-0-12-811718-7.00006-X

this is really a change of paradigm as the last author supervised both studies. It is possible to influence the mechanical properties of the heart by preventing fibrosis as much as possible. This is done by the injection of stem cells onto the heart surface; this is also known as *stem cell therapy*, which seems to be a very promising therapy after myocardial infarctions (see for instance Przybyt and Harmsen, 2013). The idea is that the stem cells secrete vascular endothelial growth factors (VEGF or TG-β), which activate the proliferation and migration of endothelial cells. These cells form the backbone of small blood vessels, which improves the blood transport to the damaged regions of the heart. Another important side effect is that they reduce the stiffness of the damaged regions of the heart so that the pumping efficacy and capacity increase without requiring too much force from the cardiocytes.

In this manuscript, we consider the process of angiogenesis in the heart, which is the formation and extension of the capillary network over the damaged regions of the heart. The migration of endothelial cells toward the damaged regions of the heart proceeds as a result of chemo- and haptotaxis. To model angiogenesis, several classes of models exist: cell-based formalisms on the small scales, in which cells are tracked on an individual basis, and continuum-based models, where cell densities in terms of number of cells per unit of volume or area are considered rather than individual cells. The small-scale models generally have a stochastic nature for cell proliferation and death, as well as for cell migration in terms of stochastic differential equations. Some cell-scale models are lattice based, that is, cells are allowed to occupy predefined regions of a lattice and migrate on minimization of a functional of (virtual) energy. These models fall within the class of cellular automata formalisms, which are very popular in modeling angiogenesis (van Oers et al., 2014). Recently a semicontinuous cell-based model has been developed for angiogenesis where cells have a certain predefined or evolving geometry (Bookholt et al., 2016).

Currently, we, however, consider angiogenesis on the continuum scale on the basis of a system of partial differential equations. To approximate the solution of partial differential equations, finite element techniques offer a large amount of freedom with respect to geometry and sudden changes of coefficients, see for instance the books Atkinson and Han (2009) and Brenner and Scott (2008). The present chapter deals with a Keller−Segel type (Byrne and Chaplain, 1995, for instance) of formalism for the migration of endothelial cells. This model is characterized by the strong dominance of the convective (first-order) term in the reaction transport equations. Furthermore, the gradient of a chemical signal, which is approximated by a numerical solution to a partial differential equation as well, has to be determined. This poses several numerical challenges because standard Galerkin methods generally need very high grid resolutions to deal with convection-dominated problems. Despite the enormous popularity of SUPG (streamline upwind Petrov−Galerkin) methods because of their ease of implementation and reliability, one has sought useful and reliable alternatives that are able to maintain a high quality of the numerical solution in terms of an accurate approximation in regions with large gradients, preferably at low computational cost and where monotonicity of the solution is preserved. As an alternative, several studies report of the application of the algebraic flux correction method to handle hyperbolic partial differential equations in a finite element setting, see for instance the study by Moller (2013). If it comes to hyperbolic equations, or equations with a high degree of hyperbolicity, then finite volume methods are very popular because slope or flux limiting procedures are relatively straightforward to implement. We refer to Leveque (2002) as a standard work in this area.

To this end, discontinuous Galerkin (DG) methods have been developed to deal with hyperbolic (convection) problems with large gradients. These methods have been combined with flux and slope limiters that enable a computationally cheap treatment of the convective terms in case of convection-dominated problems. DG methods have been developed and analyzed in many studies and for various applications with elliptic, parabolic, and predominantly hyperbolic partial differential equations. For some classical references, we cite the work by Cockburn (1997), Hesthaven and Warburton (2008), and Paillere (1996). The application and construction of limiters and filtering to remove highly oscillatory parts of the numerical solution can be found in the studies by Qiu and Shu (2005) and Mirzaee et al (2014). Particular applications of the DG method have been studied in Hesthaven and Warburton (2008). We finally remark that chemotaxis processes were modeled using DG methods by Epshteyn and Kurgonov (2008), Epshteyn and Izmirlioglu (2009), and Epshteyn (2009, 2012). The key messages of the current manuscript are as follows:

- The application of the DG method to a chemotactic snail trail model is described.
- One- and two-dimensional methods are presented on quadrilateral meshes.
- A large order of accuracy is obtained using the DG method under the use of Runge−Kutta time integration methods.

The present chapter starts with the introduction of the mathematical model and continues with the presentation of the numerical method based on a combination of slope limiting and a DG method. Subsequently, some results have been shown in terms of simulations and we end up with some discussion and conclusions. For more mathematical details, regarding exact solution representations for simple cases in which the construction is based on the method of characteristics, the interested reader is referred to Crapts (2012).

6.2 BACKGROUND ON STEM CELL THERAPY AND THE NUMERICAL METHOD

A myocardial infarction is the regional death of myocardiocytes, which are responsible for the periodic contraction of the heart muscle. The death of myocardiocytes results in a self-reparative mechanism, in which the damaged heart tissue is replaced with a fibrotic scar, which is produced by fibroblasts and myofibroblasts (see Talman and Ruskoaho, 2016). In principle this mechanism avoids rupture of the heart ventricular walls; however, a setback is that the local mechanical stiffness in the damaged parts is higher than in the undamaged regions of the heart. The increase in local stiffness of the scarred region, which hardly contributes to the contraction mechanism, frustrates the contraction mechanism of the cardiocytes that are located at other positions of the heart. This process can play a pivotal role in the development of dangerous heart rhythm disorders and sudden death of the patient (see Lazzerini et al., 2006, for instance). To transform the fibrosis-effected scar to a less stiff tissue, stem cells are injected near fibrosis-effected regions of the heart. In this stem cell therapy, the stem cells will adhere onto the fibrotic regions of the heart (see Przybyt and Harmsen, 2013). The stem cells secrete chemokines, which make the endothelial cells (note that the endothelial cells are the backbone of blood vessels (arteries)), migrate toward the fibrosis-effected region, and reestablish a capillary network in this scar-effected region of the heart muscle. This migration toward the gradient of the concentration is referred to chemotaxis or haptotaxis. This transformation makes the region less stiff and thereby the efficiency of the contraction mechanism will increase, which also leads to a mechanically less demanding environment of the cardiocytes (see Wingstrand et al., 2016). This process can thereby prevent premature death of the patient, as well as increase the patient's quality of life.

Because the migration of endothelial cells is largely determined by movement according to the gradient of the concentration of the chemokine (chemotaxis), it is necessary to determine the gradient of the chemokine. To this extent, we use order reduction, as in mixed finite element schemes, to solve for both the gradient of the concentration and the concentration itself for the chemokine. The snail trail mechanism is dealt with analogously. This approach circumvents the need of using complicated gradient reconstruction schemes, such as the ZZ-patch-based scheme. Furthermore, the migration component from chemotaxis may be much larger than the component induced by random walk. This makes the reaction transport rather hyperbolic, for which DG methods are known to be very suitable. In particular, if the solution is characterized by large spatial variations (e.g., large gradients), then DG methods are very attractive and a good alternative to standard Galerkin methods, or SUPG methods, which introduce significant numerical diffusion in the upstream direction. We also note that conservation laws that are largely hyperbolic require the conservation of signals (such as mass) to a large degree, and from this it follows that accurate discretization methods are required in terms of spatial discretization and time integration. Finite volume methods are conservative but suffer from relatively poor accuracy if classical lower-order versions are applied. In this light, DG methods can be considered as "higher-order" finite volume methods. This makes the DG methods combined with Runge−Kutta time integration methods accurate candidates. We also note that the DG methods unfortunately are characterized by large CPU times per time step.

6.3 THE MATHEMATICAL MODEL

We model angiogenesis by a *tip-sprout* system of (hyperbolic and parabolic) partial differential equations that was originally formulated by Byrne and Chaplain (1995). In this manuscript, we simplify the surface of the heart by considering a square domain of computation. We consider a domain of computation Ω with boundary $\partial\Omega$, that is fixed in time. Presently, we use an open nonempty square domain:

$$\Omega = \{(x,y)\in\mathbb{R}^2 : |x| < 1, |y| < 1\}.$$

Furthermore, the damaged domain is given by $\Omega_\delta \subset \Omega$:

$$\Omega_\delta = \{(x,y)\in\mathbb{R}^2 : |x| < \delta, |y| < \delta\}, \quad 0 < \delta < 1.$$

We assume that at $t = 0$ (t denoting time), stem cells are injected homogeneously over the damaged region. Let $m = m(t, \mathbf{x})$ denote the stem cell density at time t and location $\mathbf{x}$, then at $t = 0$, we have

$$m(0,\mathbf{x}) = \begin{cases} m_0, & \mathbf{x}\in\Omega_w, \\ 0, & \mathbf{x}\in\Omega\setminus\Omega_w. \end{cases} \tag{6.1}$$

The natural decay of the stem cells as a result of cell death and due to migration away from the heart is modeled by

$$\frac{\partial m}{\partial t} = -\beta_1 m, \tag{6.2}$$

where $\beta_1 \geq 0$ is a stem cell decay rate coefficient whose dimension is the reciprocal time. The secretion and diffusion of the chemoattractant (TG-β) by the stem cells is modeled by

$$\frac{\partial c}{\partial t} - D_1 \Delta c + \lambda c = \alpha m, \quad (t, \mathbf{x}) \in \mathbb{R}^+ \times \Omega. \tag{6.3}$$

Here $D_1 > 0$ represents the diffusion coefficient of the chemoattractant over the domain (being the heart surface), $\lambda \geq 0$ and $\alpha \geq 0$, respectively, represent the natural decay rate and the regeneration rate by the stem cells. We note that Δ represents the two-dimensional Laplacian. As the initial condition, we assume that the concentration of chemoattractants is zero and that there is no flux over the boundary of the domain, that is

$$c(0, \mathbf{x}) = 0, \quad \text{in } \Omega, \quad D_1 \frac{\partial c}{\partial n} = 0, \quad \text{on } t > 0, \quad \mathbf{x} \in \partial\Omega.$$

In the current model, we distinguish between capillary tips and sprouts. The tips are the leading edges of the sprouts. The tips, which are constituted by the leading endothelial cells, are subject to chemotaxis, random walk (diffusion), bifurcation on both existing sprouts and the tips, as well as tip−sprout anastomosis (merging). Let the tip density and sprout density, respectively, be denoted by u and ρ, both being functions of time and space. This gives the following equation:

$$\frac{\partial u}{\partial t} + \chi_1 \nabla \cdot (u \nabla c) - D_2 \Delta u = \alpha_0 \rho c + \alpha_1 H(c - \widehat{c}) u c - \beta_2 u \rho, \quad (t, \mathbf{x}) \in \mathbb{R}^+ \times \Omega. \tag{6.4}$$

The first, second, and third terms of the left-hand side of the above equation, respectively, represent the accumulation, chemotaxis, and random walk (diffusion) of the tips. The right-hand side contains bifurcation and hence arising of tips on sprouts, bifurcation at tips (hence on the leading ends), and anastomosis (merging of tips to tips or sprouts), respectively. Further $\chi_1 \geq 0$, $D_2 > 0$, α_0, $\alpha_1 \geq 0$, and $\beta_2 \geq 0$, respectively, represent the chemotactic coefficient, diffusion coefficient, sprout bifurcation rate constant, tip bifurcation rate constant, and the anastomosis rate coefficient. It is assumed that tip bifurcation only takes place if the concentration of chemoattractant exceeds a threshold value $\hat{c} \geq 0$. The function $H(.)$ represents the Heaviside function. Initially it is assumed that the number of capillary tips is zero. Furthermore, no flux is assumed over the boundary of the domain of computation, and this results in

$$u(0, \mathbf{x}) = 0, \quad \text{in } \Omega, \quad D_2 \frac{\partial u}{\partial n} - \chi_1 u \frac{\partial c}{\partial n} = 0, \quad \text{on } t > 0, \quad \mathbf{x} \in \partial\Omega.$$

The sprouts are assumed to follow the tips. They consist of *stalking* endothelial cells. One can interpret their migration as a *snail trail* in combination with random walk and hence any position in space is occupied by a sprout once was occupied by a tip cell. In the work by Byrne and Chaplain (1995), a one-dimensional case was considered. Because we consider migration of tips predominantly toward the center of the region, we extend the one-dimensional case considered to the migration of sprouts toward the center by

$$\frac{\partial \rho}{\partial t} - D_3 \Delta \rho - (D_2 \nabla u + \chi_1 u \nabla c) \cdot \frac{\mathbf{x}}{\|\mathbf{x}\|_2} + \gamma(\rho - \rho_{\text{eq}}) = 0, \quad (t, \mathbf{x}) \in \mathbb{R}^+ \times \Omega. \tag{6.5}$$

This equation is supplemented with a Dirichlet boundary condition, which reads as

$$\rho(t, \mathbf{x}) = \rho_{\text{eq}}, \quad \text{on } t > 0, \quad \mathbf{x} \in \partial\Omega. \tag{6.6}$$

As an initial condition for the sprout density ρ, we use

$$\rho(0, \mathbf{x}) = \begin{cases} 0, & \mathbf{x} \in \Omega_w, \\ \rho_{\text{eq}}, & \mathbf{x} \in \Omega \setminus \Omega_w. \end{cases} \tag{6.7}$$

We realize that this model is not the only partial differential equation-based model for angiogenesis. Maggelakis (2003, 2004) formulated an angiogenesis where hypoxia (shortage of oxygen) was included. In her model, however, tip anastomosis and branching was neglected. Furthermore, Pettet et al. (1996) considered an alternative model that incorporates tip branching and anastomosis. Their model was not based on a *snail trail* mechanism. In the next section, we describe the numerical method based on a DG method.

6.4 NUMERICAL METHOD

The standard finite element method exhibits oscillations if the contribution of chemotaxis is large with respect to the diffusive part. To this extent, an SUPG method can be used for the suppression of oscillations. The disadvantage of the SUPG method, however, is the smearing behavior of the numerical solution, in which the large gradients are approximated by gradients that are too small. Therefore, we choose to use a DG method to solve the problem. To maintain monotonicity, the DG method can be extended with a slope limiter. Although the DG method has been explained in several manuscripts, such as Cockburn (1997) and Hesthaven and Warburton (2008), we outline the method applied to the current model. Furthermore, because the two-dimensional implementation is based on the extension of the one-dimensional implementation, we start with the explanation of the one-dimensional implementation.

6.4.1 The One-Dimensional Implementation

As in other classical discretization methods, the domain of computation is divided into elements, which reduce to line segments as elements in the one-dimensional implementation. We denote the elements by $e_j = [x_{j-1/2}, x_{j+1/2}]$. Like in the standard finite element, the differential equations are multiplied by a test function and integrated by parts to obtain a weak formulation. However, unlike in the finite-element method where one integrates over the entire domain of computation, we integrate over the element e_j. We treat the three partial differential equations in three separate subsections.

6.4.1.1 The Diffusion–Reaction Equation

Before, we write the weak formulation, we split the differential equation into a system where only first-order derivatives with respect to spatial coordinates occur, to obtain the auxiliary formulation

$$\begin{aligned} &\frac{\partial c}{\partial t} + D_1 \frac{\partial q}{\partial x} + \lambda c = \alpha m, \quad \text{for } (t,x) \in \mathbb{R}^+ \times (0,1), \\ &q + \frac{\partial c}{\partial x} = 0, \quad \text{for } (t,x) \in \mathbb{R}^+ \times (0,1). \end{aligned} \tag{6.8}$$

Here q represents the flux over element boundaries, which we describe later. Note that the initial and boundary conditions are given by $c(0, x) = 0$ and $q(t, 0) = q(t, 1) = 0$. Multiplying both equations by a test function ϕ_j, and integrating by parts over the element e_j, gives the following weak form over e_j:

$$\begin{aligned} &\int_{e_j} \left(\phi_j \frac{\partial c}{\partial t} - D_1 \frac{d\phi_j}{dx} q + \lambda \phi_j c \right) dx + \left[D_1 \phi_j q \right]_{x_{j-1/2}}^{x_{j+1/2}} = \int_{e_j} \alpha \phi_j m dx, \quad \text{for } t > 0, \\ &\int_{e_j} \left(\phi_j q - \frac{d\phi_j}{dx} c \right) dx + \left[c\phi_j \right]_{x_{j-1/2}}^{x_{j+1/2}} = 0, \quad \text{for } t > 0. \end{aligned} \tag{6.9}$$

For the test function on e_j, we use Legendre polynomials up to order k, given by

$$P_n(x) = \frac{1}{2^n n!} \frac{d^n}{dx^n} \left(x^2 - 1 \right)^n, \tag{6.10}$$

and for convenience we scale the interval e_j to the reference interval $[-1, 1]$. Let x_j be the midpoint of e_j and let $\Delta x_j = x_{j+1/2} - x_{j-1/2}$, we define $r = \frac{2(x-x_j)}{\Delta x_j}$, then each integral over e_j is represented by

$$\int_{e_j} f(x) dx = \frac{\Delta x_j}{2} \int_{-1}^{1} f\left(x_j + \frac{\Delta x_j r}{2} \right) dr. \tag{6.11}$$

The above relation is used with the orthogonality of the Legendre functions, for which we have

$$\int_{-1}^{1} P_n(x) P_m(x) dx = \frac{2}{2m+1} \delta_{n,m}, \tag{6.12}$$

where $\delta_{n,m}$ represents the Kronecker Delta. On element e_j, we choose as a test function

$$\phi_j^m(x) = P_m\left(\frac{2(x-x_j)}{\Delta x_j}\right),$$

and, on e_j, the solution is approximated by

$$c(t,x) = c_h(t,x) = \sum_{\ell=0}^{k} c_l(t)\phi_j^\ell(x) = \sum_{\ell=0}^{k} c_\ell(t)P_\ell\left(\frac{2(x-x_j)}{\Delta x_j}\right), \quad \text{and } q(t,x) = q_h(t,x) = \sum_{\ell=0}^{k} q_\ell(t)P_\ell\left(\frac{2(x-x_j)}{\Delta x_j}\right).$$

It is clear from the initial condition for $c(t, x)$ that $c_\ell(0) = 0$. Furthermore, we obtain

$$\begin{aligned}
&\sum_{\ell=0}^{k} c'_\ell(t)\int_{e_j}\phi_j^m\phi_j^\ell dx - \sum_{\ell=0}^{k} D_1 q_\ell(t)\int_{e_j}\frac{d\phi_j^m}{dx}\phi_j^\ell dx + \sum_{\ell=0}^{k} c_\ell(t)\int_{e_j}\lambda\phi_j^m\phi_j^\ell dx + \left[D_1\phi_j^m q_h(t,x)\right]_{x_{j-1/2}}^{x_{j+1/2}} = \int_{e_j}\alpha\phi_j^m m dx, \quad \text{for } t>0,\\
&\sum_{\ell=0}^{k} q_\ell(t)\int_{e_j}\phi_j^m\phi_j^\ell dx - \sum_{\ell=0}^{k} c_\ell(t)\int_{e_j}\frac{d\phi_j^m}{dx}\phi_j^\ell dx + \left[c_h(t,x)\phi_j^m\right]_{x_{j-1/2}}^{x_{j+1/2}} = 0, \quad \text{for } t>0.
\end{aligned} \tag{6.13}$$

The above system of equations contains several integrals that need to be computed. Furthermore, the boundary terms need to be defined as they are multivalued. First, we define the matrices containing the integral terms. Then, we introduce the element matrices over element e_j

$$M^j_{m\ell} = \int_{e_j}\phi_j^m(x)\phi_j^\ell(x)dx = \frac{\Delta x_j}{2}\int_{-1}^{1}P_m(r)P_\ell(r)dr = \frac{\Delta x}{2m+1}\delta_{m,\ell}, \tag{6.14}$$

and

$$S^j_{m\ell} = -\int_{e_j}\phi_j^m(x)\frac{d\phi_j^\ell}{dx}(x)dx = -\int_{-1}^{1}P_m(r)P'_\ell(r)dr. \tag{6.15}$$

For the case that $k = 3$ (four polynomials), which we consider in this chapter, we obtain

$$M^j = \Delta x\cdot\begin{pmatrix} 1 & 0 & 0 & 0\\ 0 & \frac{1}{3} & 0 & 0\\ 0 & 0 & \frac{1}{5} & 0\\ 0 & 0 & 0 & \frac{1}{7}\end{pmatrix}, \quad \text{and } S^j = \begin{pmatrix} 0 & 0 & 0 & 0\\ 2 & 0 & 0 & 0\\ 0 & 2 & 0 & 0\\ 2 & 0 & 2 & 0\end{pmatrix}.$$

The boundary terms are determined using central fluxes, by

$$\begin{aligned}
\left[D_1\phi_j^m q_h(t,x)\right]_{x_{j-1/2}}^{x_{j+1/2}} &= \frac{D_1}{2}\sum_{\ell=0}^{k}\left(q_j^\ell(t)\phi_j^\ell\left(x_{j+1/2}\right) + q_{j+1}^\ell(t)\phi_{j+1}^\ell\left(x_{j+1/2}\right)\right)\phi_j^m\left(x_{j+1/2}\right)\\
&\quad - \frac{D_1}{2}\sum_{\ell=0}^{k}\left(q_j^\ell(t)\phi_j^\ell\left(x_{j-1/2}\right) + q_{j-1}^\ell(t)\phi_{j-1}^\ell\left(x_{j-1/2}\right)\right)\phi_j^m\left(x_{j-1/2}\right).
\end{aligned} \tag{6.16}$$

The same holds for

$$\begin{aligned}
\left[\phi_j^m c_h(t,x)\right]_{x_{j-1/2}}^{x_{j+1/2}} &= \frac{1}{2}\sum_{\ell=0}^{k}\left(c_j^\ell(t)\phi_j^\ell\left(x_{j+1/2}\right) + c_{j+1}^\ell(t)\phi_{j+1}^\ell\left(x_{j+1/2}\right)\right)\phi_j^m\left(x_{j+1/2}\right)\\
&\quad - \frac{1}{2}\sum_{\ell=0}^{k}\left(c_j^\ell(t)\phi_j^\ell\left(x_{j-1/2}\right) + c_{j-1}^\ell(t)\phi_{j-1}^\ell\left(x_{j-1/2}\right)\right)\phi_j^m\left(x_{j-1/2}\right).
\end{aligned} \tag{6.17}$$

Note that D_1 is constant. As an alternative, one may use an upwind flux. In the above relations, we use $\phi_j^{\ell}(x_{j+1/2}) = P_{\ell}(1) = 1$ and $\phi_j^{\ell}(x_{j-1/2}) = P_{\ell}(-1) = (-1)^{\ell}$ to get the resulting discretization matrices, to obtain

$$\left[\phi_j^m c_h(t,x)\right]_{x_{j-1/2}}^{x_{j+1/2}} = A\mathbf{c}_{j-1} - B\mathbf{c}_{j-1} + C\mathbf{c}_{j+1}, \tag{6.18}$$

where

$$\begin{cases} A = \dfrac{1}{2}\begin{pmatrix} 1 & 1 & 1 & 1 \\ 1 & 1 & 1 & 1 \\ 1 & 1 & 1 & 1 \\ 1 & 1 & 1 & 1 \end{pmatrix} - \dfrac{1}{2}\begin{pmatrix} 1 & -1 & 1 & -1 \\ -1 & 1 & -1 & 1 \\ 1 & -1 & 1 & -1 \\ 1 & -1 & 1 & -1 \end{pmatrix}, \\ B = \dfrac{1}{2}\begin{pmatrix} 1 & 1 & 1 & 1 \\ -1 & -1 & -1 & -1 \\ 1 & 1 & 1 & 1 \\ -1 & -1 & -1 & -1 \end{pmatrix}, \quad C = \dfrac{1}{2}\begin{pmatrix} 1 & -1 & 1 & -1 \\ 1 & -1 & 1 & -1 \\ 1 & -1 & 1 & -1 \\ 1 & -1 & 1 & -1 \end{pmatrix}. \end{cases}$$

Furthermore, we use the convention

$$\mathbf{c}_j(t) = \left[c_j^0(t)\ldots c_j^k(t)\right]^T, \quad \text{and } \mathbf{q}_j(t) = \left[q_j^0(t)\ldots q_j^k(t)\right]^T,$$

which are the vectors with degrees of freedom on element e_j. The procedure is similar for the q-term. The right-hand side is given by

$$\int_{e_j} \alpha\phi_j^m m dx = \alpha\frac{\Delta x_j}{2}\int_{-1}^{1} m\left(t, x_j + \frac{\Delta x_j r}{2}\right)P_m(r)dr = \alpha\frac{\Delta x_j}{2}m(t,x_j)\int_{-1}^{1} P_m(r)dr. \tag{6.19}$$

Here we used that $m(t, x)$ is constant over the element e_j. This implies that

$$f_j(t) = \frac{\Delta x_j}{2}\alpha m(t,x_j)\begin{pmatrix} 2 \\ 0 \\ 0 \\ 0 \end{pmatrix}.$$

Now we have all the ingredients to set up the following system of ordinary differential equations to be integrated over time:

$$\begin{aligned} M\frac{d\mathbf{c}_j(t)}{dt} &= D_1(A-S)\mathbf{q}_j - D_1 B\mathbf{q}_{j+1} - \lambda M\mathbf{c}_j + \mathbf{f}_j, \\ M\mathbf{q}_j &= (A-S)\mathbf{c}_j - B\mathbf{c}_{j-1} + C\mathbf{c}_{j+1}. \end{aligned} \tag{6.20}$$

The above system is integrated using a third-order total variation diminishing (TVD) Runge−Kutta method Gottlieb and Shu (1998). For a semidiscrete scheme, given by

$$\frac{du}{dt} = L(u),$$

this gives

$$\begin{aligned} u^{(1)} &= u^n + \Delta t L(u^n), \\ u^{(2)} &= \frac{3}{4}u^n + \frac{1}{4}u^{(1)} + \frac{1}{4}\Delta t L\big(u^{(1)}\big), \\ u^{n+1} &= \frac{1}{3}u^n + \frac{2}{3}u^{(2)} + \frac{2}{3}\Delta t L\big(u^{(2)}\big). \end{aligned} \tag{6.21}$$

The discretization in space using DG has the advantage that it is able to handle complicated geometries and arbitrary triangulations. Using a TVD scheme, such as RK3-TVD, has the advantage that it can compute approximations, which are either smooth or have weak shocks and other discontinuities, without any further modification. Hence, discontinuities may become smeared in future time steps; however, eventually, they will not become oscillatory. If, however, the discontinuities are too strong, then oscillations and even nonlinear instability can occur. To avoid both these nuisances, a slope limiter, such as the minmod limiter, can be applied.

6.4.1.2 The Tips Equation

Subsequently, we deal with the one-dimensional chemotaxis−diffusion−reaction equation, given by

$$\frac{\partial u}{\partial t} + \chi_1 \frac{\partial}{\partial x}(uq) - D_2 \frac{\partial w}{\partial x} = uF(c,\rho) + \alpha_0 \rho c, \tag{6.22}$$

where two of the reactive terms have been simplified to a single function $F(c, \rho)$. Further, $q + \frac{\partial c}{\partial x} = 0$ and

$$w + \frac{\partial u}{\partial x} = 0.$$

Multiplication of the equations by test function ϕ_j and integrating (by parts) over element e_j gives

$$\begin{aligned} &\int_{e_j} \phi_j \frac{\partial u}{\partial t} dx + \int_{e_j} \chi_1 uq \frac{d\phi_j}{dx} dx - \int_{e_j} D_2 w \frac{d\phi_j}{dx} dx - \big[\chi_1 uq\phi_j\big]_{x_{j-\frac{1}{2}}}^{x_{j+\frac{1}{2}}} + \big[D_2 w\phi_j\big]_{x_{j-\frac{1}{2}}}^{x_{j+\frac{1}{2}}} = \int_{e_j} \big(\phi_j uF(c,\rho) + \alpha_0\rho c\big)dx, \\ &\int_{e_j} w\phi_j dx - \int_{e_j} u \frac{d\phi_j}{dx} dx - \big[\phi_j u\big]_{x_{j-\frac{1}{2}}}^{x_{j+\frac{1}{2}}} = 0. \end{aligned} \tag{6.23}$$

Subsequently, as in the previous subsection, we write the solution u in terms of the basis functions, that is, as

$$u(t,x) \approx u_h(t,x) = \sum_{\ell=0}^{k} u_j^\ell(t)\phi_j^\ell(x), \quad w(t,x) \approx w_h(t,x) = \sum_{\ell=0}^{k} w_j^\ell(t)\phi_j^\ell(x),$$

over element e_j and we set $\phi_j = \phi_j^m$, for $m = 0,\ldots,k$, to obtain

$$\begin{aligned} &\sum_{\ell=0}^{k} \frac{du_j^\ell(t)}{dt} \int_{e_j} \phi_j^m \phi_j^\ell dx + \sum_{\ell=0}^{k} u_j^\ell(t) \int_{e_j} \chi q \phi_j^\ell \frac{d\phi_j^m}{dx} dx - \sum_{\ell=0}^{k} w_j^\ell(t) \int_{e_j} D_2 \frac{d\phi_j^m}{dx} \phi_j^\ell dx - \Big[\chi (qu)^* \phi_j^m\Big]_{x_{j-\frac{1}{2}}}^{x_{j+\frac{1}{2}}} \\ &+ \Big[D_2 w^* \phi_j^m\Big]_{x_{j-\frac{1}{2}}}^{x_{j+\frac{1}{2}}} = \sum_{\ell=0}^{k} u_j^\ell(t) \int_{e_j} \phi_j^m \phi_j^\ell F(c,\rho) dx + \int_{e_j} \alpha_0 \rho c dx, \\ &\sum_{\ell=0}^{k} w_j^\ell(t) \int_{e_j} \phi_j^m \phi_j^\ell dx - \sum_{\ell=0}^{k} u_j^\ell(t) \int_{e_j} \frac{d\phi_j^m}{dx} \phi_j^\ell dx + \sum_{\ell=0}^{k} u_j^\ell(t) \Big[\phi_j^m \phi_j^\ell\Big]_{x_{j-\frac{1}{2}}}^{x_{j+\frac{1}{2}}} = 0. \end{aligned} \tag{6.24}$$

All terms in the above equations are dealt with analogously to the treatment in the previous subsection. Except for the boundary terms, which are treated using the local Lax−Friedrich flux (which is a central flux with an additional stabilization term), this gives

$$\begin{aligned}
\left[w^*\phi_j^m\right]_{x_{j-\frac{1}{2}}}^{x_{j+\frac{1}{2}}} &= \frac{1}{2}\sum_{\ell=0}^{k}\left(w_j^\ell(t)\phi_j^\ell\left(x_{j+\frac{1}{2}}\right)+w_{j+1}^\ell(t)\phi_{j+1}^\ell\left(x_{j+\frac{1}{2}}\right)\right)\phi_j^m\left(x_{j+\frac{1}{2}}\right)\\
&\quad-\frac{1}{2}\sum_{\ell=0}^{k}\left(w_j^\ell(t)\phi_j^\ell\left(x_{j-\frac{1}{2}}\right)+w_{j-1}^\ell(t)\phi_{j-1}^\ell\left(x_{j-\frac{1}{2}}\right)\right)\phi_j^m\left(x_{j-\frac{1}{2}}\right),\\
\left[(uq)^*\phi_j^m\right]_{x_{j-\frac{1}{2}}}^{x_{j+\frac{1}{2}}} &= \frac{1}{2}\sum_{\ell=0}^{k}\left(u_j^\ell(t)\phi_j^\ell\left(x_{j+\frac{1}{2}}\right)+u_{j+1}^\ell(t)\phi_{j+1}^\ell\left(x_{j+\frac{1}{2}}\right)\right)q\left(t,x_{j+\frac{1}{2}}\right)\phi_j^m\left(x_{j+\frac{1}{2}}\right)\\
&\quad-\frac{1}{2}\sum_{\ell=0}^{k}\left(u_j^\ell(t)\phi_j^\ell\left(x_{j-\frac{1}{2}}\right)+u_{j-1}^\ell(t)\phi_{j-1}^\ell\left(x_{j-\frac{1}{2}}\right)\right)q\left(t,x_{j-\frac{1}{2}}\right)\phi_j^m\left(x_{j-\frac{1}{2}}\right)-\left[\frac{z}{2}[[u]]\right]_{x_{j-\frac{1}{2}}}^{x_{j+\frac{1}{2}}},\\
\left[u^*\phi_j^m\right]_{x_{j-\frac{1}{2}}}^{x_{j+\frac{1}{2}}} &= \frac{1}{2}\sum_{\ell=0}^{k}\left(u_j^\ell(t)\phi_j^\ell\left(x_{j+\frac{1}{2}}\right)+u_{j+1}^\ell(t)\phi_{j+1}^\ell\left(x_{j+\frac{1}{2}}\right)\right)\phi_j^m\left(x_{j+\frac{1}{2}}\right)\\
&\quad-\frac{1}{2}\sum_{\ell=0}^{k}\left(u_j^\ell(t)\phi_j^\ell\left(x_{j-\frac{1}{2}}\right)+u_{j-1}^\ell(t)\phi_{j-1}^\ell\left(x_{j-\frac{1}{2}}\right)\right)\phi_j^m\left(x_{j-\frac{1}{2}}\right),
\end{aligned}\tag{6.25}$$

where

$$\begin{aligned}
\left[\left[u\left(t,x_{j+\frac{1}{2}}\right)\right]\right] &= u_j\left(t,x_{j+\frac{1}{2}}\right)-u_{j+1}\left(t,x_{j+\frac{1}{2}}\right),\\
\left[\left[u\left(t,x_{j-\frac{1}{2}}\right)\right]\right] &= u_j\left(t,x_{j-\frac{1}{2}}\right)-u_{j-1}\left(t,x_{j-\frac{1}{2}}\right),\\
z\left(x_{j-\frac{1}{2}}\right) &= \max\left\{\left|q_j\left(t,x_{j-\frac{1}{2}}\right)\phi_j^m\left(x_{j-\frac{1}{2}}\right)\right|,\left|q_{j-1}\left(t,x_{j-\frac{1}{2}}\right)\phi_{j-1}^m\left(x_{j-\frac{1}{2}}\right)\right|\right\},\\
z\left(x_{j+\frac{1}{2}}\right) &= \max\left\{\left|q_j\left(t,x_{j+\frac{1}{2}}\right)\phi_j^m\left(x_{j+\frac{1}{2}}\right)\right|,\left|q_{j+1}\left(t,x_{j+\frac{1}{2}}\right)\phi_{j+1}^m\left(x_{j+\frac{1}{2}}\right)\right|\right\}.
\end{aligned}\tag{6.26}$$

Substituting $r=\frac{2(x-x_j)}{\Delta x_j}$, and using the Legendre polynomials with Gauss−Legendre quadrature, we introduce

$$\begin{aligned}
V_{1j,ml} &= \sum_{i=1}^{6}\chi q\left(t,x_j+\frac{\Delta x_j}{2}r_i\right)P_l(r_i)\frac{dP_m(r)}{dt}w_i,\\
V_{2j,ml} &= \sum_{i=1}^{6}\frac{\Delta x_j}{2}P_l(r_i)P_m(r_i)F\left(c\left(t,x_j+\frac{\Delta x_j}{2}r_i\right),\rho\left(t,x_j+\frac{\Delta x_j}{2}r_i\right)\right)w_i,\\
V_{3j,m} &= \sum_{i=1}^{6}\frac{\Delta x_j}{2}\alpha_0\rho\left(t,x_j+\frac{\Delta x_j}{2}r_i\right)c\left(t,x_j+\frac{\Delta x_j}{2}r_i\right)P_m(r_i)w_i,\\
\left[\chi(uq)^*\phi_j^m\right]_{x_{j-\frac{1}{2}}}^{x_{j+\frac{1}{2}}} &= (C\mathbf{u}_{j+1}+A_1\mathbf{u}_j)\sum_{\ell=0}^{k}q_j^\ell P_\ell(1)-(A_2\mathbf{u}_j+B\mathbf{u}_{j-1})\sum_{\ell=0}^{k}q_j^\ell P_\ell(-1).
\end{aligned}\tag{6.27}$$

TABLE 6.1 Six Points and Their Weights for the Gauss–Legendre Quadrature

Points	Weights
±0.23861918	0.46791393
±0.66120939	0.36076157
±0.93246951	0.17132449

Here we used the Gauss–Legendre points from Table 6.1.

The numerical approximation for the coefficients using DG for the one-dimensional form can be developed now. Therewith, we get

$$M\frac{d\mathbf{u}_j}{dt} = D_2(A-S)\mathbf{w}_j + \mathbf{q}_j - D_2B\mathbf{w}_{j-1} + D_2C\mathbf{w}_{j+1} + (V_{1j}+V_{2j})\mathbf{u}_j + V_{3j}$$
$$-\chi\left((C\mathbf{u}_{j+1}+A_1\mathbf{u}_j)\sum_{\ell=0}^{k}q_j^{\ell}(t)P_{\ell}(1) - (A_2\mathbf{u}_j+B\mathbf{u}_{j-1})\sum_{\ell=0}^{k}q_j^{\ell}(t)P_{\ell}(-1)\right), \tag{6.28}$$

$$M\mathbf{w}_j = (A-S)\mathbf{u}_j - B\mathbf{u}_{j-1} + C\mathbf{u}_{j+1}.$$

The above system is, as in the previous section, also integrated over time using the third-order TVD Runge–Kutta method.

6.4.1.3 The Vessel Density

The vessel equation is rewritten using $q = -\frac{\partial c}{\partial x}$, $w = -\frac{\partial u}{\partial x}$ to obtain

$$\frac{\partial \rho}{\partial t} + D_3\frac{\partial v}{\partial x} + \mu_1 w - \chi_1 uq + \gamma(\rho - \rho_{\text{eq}}) = 0,$$
$$v + \frac{\partial \rho}{\partial x} = 0. \tag{6.29}$$

The above equation is subject to initial and boundary conditions

$$\rho(0,x) = \begin{cases} 0, & x\in\Omega_w, \\ \rho_{\text{eq}}, & x\in\Omega\setminus\Omega_w, \end{cases} \tag{6.30}$$
$$v(t,0) = 0,\ \ \rho(t,1) = \rho_{\text{eq}}.$$

The numerical solution is determined by

$$\rho(t,x)\approx\rho_h(t,x) = \sum_{\ell=0}^{k}\rho_j^{\ell}(t)\phi_j^{\ell}(x),$$

and

$$v(t,x)\approx v_h(t,x) = \sum_{\ell=0}^{k}v_j^{\ell}(t)\phi_j^{\ell}(x).$$

Using the orthogonal structure of the Legendre polynomials, we determine the initial coefficients in the numerical solution by

$$\rho_j^m(0) = \frac{2m+1}{2}\int_{-1}^{1}\rho\left(0, x_j+\frac{\Delta x}{2}r\right)P_m(r)dr \approx \frac{2m+1}{2}\sum_{i=1}^{6}\rho\left(0, x_j+\frac{\Delta x}{2}r_i\right)P_m(r_i)w_i. \tag{6.31}$$

To determine the weak formulation, we multiply the equations by ϕ_j and integrate over the element e_j. Integration by parts gives

$$\begin{aligned}
&\int_{e_j}\left(\frac{\partial\rho}{\partial t}\phi_j - D_3 v\frac{d\phi_j}{dx} + \mu_1 w\phi_j - \chi_1 uq\phi_j + \gamma(\rho-\rho_{\text{eq}})\phi_j\right)dx + \left[D_3 v\phi_j\right]_{x_{j-\frac{1}{2}}}^{x_{j+\frac{1}{2}}} = 0,\\
&\int_{e_j}\left(v\phi_j - \rho\frac{d\phi_j}{dx}\right)dx + \left[\rho\phi_j\right]_{x_{j-\frac{1}{2}}}^{x_{j+\frac{1}{2}}} = 0.
\end{aligned} \tag{6.32}$$

Substitution of $\rho(t,x)\approx\rho_h(t,x) = \sum_{\ell=0}^{k}\rho_j^l(t)\phi_j^\ell(x)$ and $v(t,x)\approx v_h(t,x) = \sum_{\ell=0}^{k}v_j^\ell(t)\phi_j^\ell(x)$ and $\phi_j = \phi_j^m$ gives the following Galerkin equations:

$$\begin{aligned}
&\sum_{\ell=0}^{k}\frac{d\rho_j^\ell(t)}{dt}\int_{e_j}\phi_j^m\phi_j^\ell dx - D_3\sum_{\ell=0}^{k}v_j^\ell(t)\int_{e_j}\frac{d\phi_j^m}{dx}\phi_j^\ell dx + \left[D_3 v^*\phi_j^m\right]_{x_{j-\frac{1}{2}}}^{x_{j+\frac{1}{2}}} + \gamma\sum_{l=0}^{k}\rho_j^l(t)\int_{e_j}\phi_j^m\phi_j^l dx = \int_{e_j}(\chi_1 uq - \mu_1 w + \gamma\rho_{\text{eq}})\phi_j^m dx,\\
&\sum_{\ell=0}^{k}u_j^\ell(t)\int_{e_j}\phi_j^m\phi_j^\ell dx - \sum_{\ell=0}^{k}\rho_j^\ell(t)\int_{e_j}\frac{\partial\phi_j^m}{dx}\phi_j^\ell dx + \left[\rho^*\phi_j^m\right]_{x_{j-\frac{1}{2}}}^{x_{j+\frac{1}{2}}} = 0.
\end{aligned} \tag{6.33}$$

Here we use the central fluxes

$$\begin{aligned}
\left[v^*\phi_j^m\right]_{x_{j-\frac{1}{2}}}^{x_{j+\frac{1}{2}}} &= \frac{1}{2}\left(\sum_{\ell=0}^{k}u_j^\ell(t)\phi_j^\ell\left(x_{j+\frac{1}{2}}\right) + u_{j+1}^\ell(t)\phi_{j+1}^\ell\left(x_{j+\frac{1}{2}}\right)\right)\phi_j^m\left(x_{j+\frac{1}{2}}\right)\\
&\quad - \frac{1}{2}\left(\sum_{\ell=0}^{k}u_j^\ell(t)\phi_j^\ell\left(x_{j-\frac{1}{2}}\right) + u_{j-1}^\ell(t)\phi_{j-1}^\ell\left(x_{j-\frac{1}{2}}\right)\right)\phi_j^m\left(x_{j-\frac{1}{2}}\right),\\
\left[\rho^*\phi_j^m\right]_{x_{j-\frac{1}{2}}}^{x_{j+\frac{1}{2}}} &= \frac{1}{2}\left(\sum_{\ell=0}^{k}\rho_j^\ell(t)\phi_j^\ell\left(x_{j+\frac{1}{2}}\right) + \rho_{j+1}^\ell(t)\phi_{j+1}^\ell\left(x_{j+\frac{1}{2}}\right)\right)\phi_j^m\left(x_{j+\frac{1}{2}}\right)\\
&\quad - \frac{1}{2}\left(\sum_{\ell=0}^{k}\rho_j^\ell(t)\phi_j^\ell\left(x_{j-\frac{1}{2}}\right) + \rho_{j-1}^\ell(t)\phi_{j-1}^\ell\left(x_{j-\frac{1}{2}}\right)\right)\phi_j^m\left(x_{j-\frac{1}{2}}\right).
\end{aligned} \tag{6.34}$$

Substituting $r = \frac{2(x-x_j)}{\Delta x_j}$, using Legendre polynomials and using Gauss−Legendre quadrature, we arrive at

$$\begin{aligned}
\mathbf{g}_{1j,m} &= \frac{\Delta x_j}{2}\int_{-1}^{1}\gamma\rho_{\text{eq}}P_m(r)dr \Rightarrow \mathbf{g}_{1j} = \frac{\Delta x_j}{2}\gamma\rho_{\text{eq}}\begin{bmatrix}2 & 0 & 0 & 0\end{bmatrix}^T,\\
\mathbf{g}_{2j,m} &= \mu_1\frac{\Delta x_j}{2}\sum_{i=1}^{6}w\left(t, x_j+\frac{\Delta x_j}{2}r_i\right)P_m(r_i)w_i,\\
\mathbf{g}_{3j,m} &= \chi_1\frac{\Delta x_j}{2}\sum_{i=1}^{6}u\left(t, x_j+\frac{\Delta x_j}{2}r_i\right)q\left(t, x_j+\frac{\Delta x_j}{2}r_i\right)P_m(r_i)w_i.
\end{aligned} \tag{6.35}$$

Here j represents the element number. Further four Legendre polynomials are used, hence up to third order, and the weights from Table 6.1 are used, such that

$$\mathbf{g}_j = \mathbf{g}_{1j} + \mathbf{g}_{2j} - \mathbf{g}_{3j}, \tag{6.36}$$

which is substituted to get the system of ordinary differential equations that is integrated over time. The system reads as

$$\begin{aligned} M\frac{d\rho_j}{dt} &= D_3(A-S)\mathbf{u}_j - D_3B\mathbf{u}_{j-1} + D_3C\mathbf{u}_{j+1} - \gamma M\rho_j + \mathbf{g}_j, \\ M\mathbf{u}_j &= (A-S)\rho_j - B\rho_{j-1} + C\rho_{j+1}. \end{aligned} \tag{6.37}$$

The above system is also integrated using the third-order TVD Runge−Kutta time integration scheme.

6.4.2 Extension to Two Spatial Dimensions

We extended the formalism and method to circular symmetry so that the problem remains quasi one-dimensional with respect to space. We refer to the MSc thesis written by Crapts for the results. In this section, the genuine 2D case for rectangular geometry is presented. This gives the freedom to deal with various geometries of the damage. The rectangular domain has been partitioned into rectangular elements, where we use N and M elements in the x and y directions. The elements are denoted by e_{ij}, with dimensions $\Delta x\Delta y$, and Legendre polynomials up to order k per coordinate direction are used as basis functions on each element. This implies that per element we have $(k+1)\times(k+1)$ polynomials and unknowns. Let P_j be the jth order Legendre polynomial, then for each element the following set of basis functions is used:

$$\mathbb{P}^k = \{P_pP_q : (p,q) \in \{0,\ldots,k\}\times\{0,\ldots,k\}\}. \tag{6.38}$$

To solve the equations by the 2D DG method, we will start reducing the order of spatial derivatives to one again as in the 1D case.

6.4.2.1 The Concentration Equation

The equation for the 2D concentration is rewritten by

$$\begin{aligned} \frac{\partial c}{\partial t} + D_1\nabla\cdot\mathbf{q} + \lambda c &= \alpha m, \\ \mathbf{q} + \nabla c &= 0. \end{aligned} \tag{6.39}$$

The solution vector $\mathbf{q}$ is written as $\mathbf{q} = [q_1\ q_2]^T$ is terms of its components. First the weak form is derived by multiplication by a test function ϕ_{ij}, integration over element e_{ij}, and subsequent integration by parts. One arrives at

$$\begin{aligned} &\int_{e_{ij}} \phi_{ij}\frac{\partial c}{\partial t} - D_1\mathbf{q}\cdot\nabla\phi_{ij} + \lambda\phi_{ij}c\,d\Omega + \int_{\partial e_{ij}} D_1\phi_{ij}\mathbf{q}\cdot n\,d\Gamma = \int_{e_{ij}} \alpha\phi_{ij}m\,d\Omega, \\ &\int_{e_{ij}} \phi_{ij}q_1 - c\frac{\partial\phi_{ij}}{\partial x}d\Omega + \int_{\partial e_{ij}} c\phi_{ij}n_1\,d\Gamma = 0, \\ &\int_{e_{ij}} \phi_{ij}q_2 - c\frac{\partial\phi_{ij}}{\partial y}d\Omega + \int_{\partial e_{ij}} c\phi_{ij}n_2\,d\Gamma = 0, \end{aligned} \tag{6.40}$$

where n_1 and n_2, respectively, denote the x and y components of the outward pointing unit normal vector. Note that we wrote the weak form per component. The test function is written as $\phi_{ij}(x,y) = \phi_i^{(m_x)}(x)\phi_j^{(m_y)}(y)$ and the solution is approximated by

$$c(t,x,y) \approx c_h(t,x,y) = \sum_{\ell_x=0}^{k}\sum_{\ell_y=0}^{k} c_{ij}^{(\ell_x,\ell_y)}(t)\phi_i^{(\ell_x)}(x)\phi_i^{(\ell_y)}(y).$$

From the initial condition, we have $c_{ij}^{(\ell_x,\ell_y)} = 0$. Substitution of the test function and numerical solution gives the following Galerkin equations over element e_{ij}:

$$\begin{aligned}
&\sum_{\ell_x=0}^{k}\sum_{\ell_y=0}^{k}\frac{dc_{ij}^{(\ell_x,\ell_y)}}{dt}\int_{e_{ij}}\phi_i^{(\ell_x)}\phi_j^{(\ell_y)}\phi_i^{(m_x)}\phi_i^{(m_y)}d\Omega + D_1\sum_{\ell_x=0}^{k}\sum_{\ell_y=0}^{k}q_{1_{ij}}^{(\ell_x,\ell_y)}\int_{e_{ij}}\phi_i^{(\ell_x)}\phi_j^{(\ell_y)}\frac{d\phi_i^{(m_x)}}{dx}\phi_i^{(m_y)}d\Omega \\
&+ D_1\sum_{\ell_x=0}^{k}\sum_{\ell_y=0}^{k}q_{2_{ij}}^{(\ell_x,\ell_y)}\int_{e_{ij}}\phi_i^{(l_x)}\phi_j^{(l_y)}\phi_i^{(m_x)}\frac{d\phi_i^{(m_y)}}{dy}d\Omega + \sum_{\ell_x=0}^{k}\sum_{\ell_y=0}^{k}\lambda c_{ij}^{(\ell_x,\ell_y)}\int_{e_{ij}}\phi_i^{(\ell_x)}\phi_j^{(\ell_y)}\phi_i^{(m_x)}\phi_i^{(m_y)}d\Omega \\
&- \int_{\partial e_{ij}} D_1\left(q_1^* n_x + q_2^* n_y\right)\phi_i^{(m_x)}\phi_j^{(m_y)}d\Gamma = \alpha\int_{e_{ij}} m(t,x,y)\phi_i^{(m_x)}\phi_j^{(m_y)}d\Omega, \\
&\sum_{\ell_x=0}^{k}\sum_{\ell_y=0}^{k}q_{1_{ij}}^{(\ell_x,\ell_y)}\int_{e_{ij}}\phi_i^{(\ell_x)}\phi_j^{(\ell_y)}\phi_i^{(m_x)}\phi_i^{(m_y)}d\Omega \\
&- \sum_{\ell_x=0}^{k}\sum_{\ell_y=0}^{k}c_{ij}^{(\ell_x,\ell_y)}\int_{e_{ij}}\phi_i^{(\ell_x)}\phi_j^{(\ell_y)}\frac{d\phi_i^{(m_x)}}{dx}\phi_i^{(m_y)}d\Omega + \int_{\partial e_{ij}} c^* n_x\phi_i^{(m_x)}\phi_j^{(m_y)}d\Gamma = 0, \\
&\sum_{\ell_x=0}^{k}\sum_{\ell_y=0}^{k}q_{2_{ij}}^{(\ell_x,\ell_y)}\int_{e_{ij}}\phi_i^{(\ell_x)}\phi_j^{(\ell_y)}\phi_i^{(m_x)}\phi_i^{(m_y)}d\Omega \\
&- \sum_{\ell_x=0}^{k}\sum_{\ell_y=0}^{k}c_{ij}^{(\ell_x,\ell_y)}\int_{e_{ij}}\phi_i^{(\ell_x)}\phi_j^{(\ell_y)}\phi_i^{(m_x)}\frac{d\phi_j^{(m_y)}}{dy}d\Omega + \int_{\partial e_{ij}} c^* n_y\phi_i^{(m_x)}\phi_j^{(m_y)}d\Gamma = 0, \\
&(m_x,m_y)\in\{0,\ldots,l\}\times\{0,\ldots,k\}.
\end{aligned} \tag{6.41}$$

Here we use the central flux in the both the x and y directions. For the test functions, we use Legendre polynomials and we use the dimensionless coordinates $r = \frac{2(x-x_i)}{\Delta x}$ and $s = \frac{2(y-y_i)}{\Delta y}$ and transformed functions $\phi_i^{(\ell_x)}\left(x_i + \frac{\Delta x}{2}r\right) = P_{\ell_x}(r)$ and $\phi_j^{(\ell_y)}\left(y_j + \frac{\Delta y}{2}s\right) = P_{\ell_y}(s)$. Substitution, integration, and using the orthogonality relations give

$$\begin{aligned}
M_{m\ell} &= \frac{\Delta x}{2}\frac{\Delta y}{2}\int_{-1}^{1}\int_{-1}^{1}P_{\ell_x}P_{\ell_y}P_{m_x}P_{m_y}drds = \frac{\Delta x\Delta y}{(2\ell_x+1)(2\ell_y+1)}\delta_{m_x,\ell_x}\delta_{m_y,\ell_y}, \\
S_{\mathbf{x},m\ell} &= \frac{\Delta y}{2}\int_{-1}^{1}\int_{-1}^{1}P_{\ell_x}P_{\ell_y}\frac{dP_{m_x}}{dr}P_{m_y}drds = \frac{\Delta y}{2\ell_y+1}\delta_{m_y,\ell_y}\int_{-1}^{1}P_{\ell_x}\frac{dP_{m_x}}{dr}dr, \\
S_{\mathbf{y},m\ell} &= \frac{\Delta x}{2}\int_{-1}^{1}\int_{-1}^{1}P_{\ell_x}P_{\ell_y}P_{m_x}\frac{dP_{m_y}}{ds}drds = \frac{\Delta y}{2\ell_y+1}\delta_{m_y,\ell_y}\int_{-1}^{1}P_{\ell_x}\frac{dP_{m_x}}{ds}ds
\end{aligned} \tag{6.42}$$

Because we use $k = 2$, we get

$$S_{\mathbf{x}} = \begin{pmatrix} 0 & 0 & 0 & 0 & 0 & 0 & 0 & 0 & 0 \\ 2 & 0 & 2 & 0 & 0 & 2 & 0 & 0 & 0 \\ 0 & 0 & 0 & 0 & 0 & 0 & 0 & 0 & 0 \\ 2 & 0 & 2 & 0 & 0 & 2 & 0 & 0 & 0 \\ 0 & 2 & 0 & 2 & 0 & 0 & 0 & 2 & 0 \\ 0 & 0 & 0 & 0 & 0 & 0 & 0 & 0 & 0 \\ 0 & 2 & 0 & 2 & 0 & 0 & 0 & 2 & 0 \\ 2 & 0 & 2 & 0 & 0 & 2 & 0 & 0 & 0 \\ 0 & 2 & 0 & 2 & 0 & 0 & 0 & 2 & 0 \end{pmatrix}, \quad S_{\mathbf{y}} = \begin{pmatrix} 0 & 0 & 0 & 0 & 0 & 0 & 0 & 0 & 0 \\ 0 & 0 & 0 & 0 & 0 & 0 & 0 & 0 & 0 \\ 2 & 2 & 0 & 0 & 2 & 0 & 0 & 0 & 0 \\ 2 & 2 & 0 & 0 & 2 & 0 & 0 & 0 & 0 \\ 0 & 0 & 0 & 0 & 0 & 0 & 0 & 0 & 0 \\ 0 & 0 & 2 & 2 & 0 & 0 & 2 & 0 & 0 \\ 2 & 2 & 0 & 0 & 2 & 0 & 0 & 2 & 0 \\ 0 & 0 & 2 & 2 & 0 & 0 & 2 & 0 & 0 \\ 0 & 2 & 2 & 2 & 0 & 0 & 2 & 0 & 0 \end{pmatrix} \tag{6.43}$$

The right-hand side becomes

$$\mathbf{f}_{ij} = \frac{\Delta x}{2}\frac{\Delta y}{2}\alpha m(t, x_i, y_j)\cdot[40\ldots0]^T. \tag{6.44}$$

Subsequently, we consider the flux terms. As an example, we write out the "c-term":

$$\int_{\partial e_{ij}} c^* n_x \phi_i^{(m_x)} \phi_i^{(m_y)} d\Gamma = \frac{\Delta y}{2(2l_y+1)} \sum_{\ell_x=0}^{k} \sum_{\ell_y=0}^{k} \left\{ c_{ij}^{(\ell_x,\ell_y)} + (-1)^{\ell_x} c_{i+1,j}^{(\ell_x,\ell_y)} - (-1)^{\ell_x}(-1)^{m_x} c_{ij}^{(\ell_x,\ell_y)} - (-1)^{m_x} c_{i-1,j}^{(\ell_x,\ell_y)} \right\}. \tag{6.45}$$

Analogously to the 1D case, we can assemble all the equations into a matrix-vector format. The resulting system of ordinary differential equations is integrated over time using the third-order TVD Runge−Kutta integration method. More details have been given in Crapts (2012).

6.4.2.2 The Tips Equation

Reducing the order of the spatial derivatives using $\mathbf{w} = -\nabla u$ gives

$$\begin{aligned} \frac{\partial u}{\partial t} + \chi_1 \nabla\cdot(u\mathbf{q}) - D_2 \nabla\cdot\mathbf{w} &= uF(c,\rho) + \alpha_0 \rho c, \\ \mathbf{w} + \nabla u &= 0. \end{aligned} \tag{6.46}$$

The weak form has been derived several before, and, also for the 1D case of the equation, this has already been presented in this manuscript. Therefore, we omit the weak form here. The most important issue is the way the flux equation as an integration over the boundary of an element is treated. This gives the coupling between adjacent elements. The hyperbolic nature as a result of the chemotaxis term necessitates us to use a central flux with an additional stabilization term, so that we get

$$\begin{aligned} \int_{\partial e_{ij}} u^* q_1 \phi_i^{(m_x)} \phi_j^{(m_y)} n_x d\Gamma &= \int_{y_{j-\frac{1}{2}}}^{y_{j+\frac{1}{2}}} \left[u^* q_1 \phi_i^{(m_x)} \phi_j^{(m_y)} \right]_{x_{i-\frac{1}{2}}}^{x_{i+\frac{1}{2}}} d\Gamma \\ &= \int_{y_{j-\frac{1}{2}}}^{y_{j+\frac{1}{2}}} u\left(t, x_{i+\frac{1}{2}}, y\right) q_1\left(t, x_{i+\frac{1}{2}}, y\right) \phi_i^{(m_x)}\left(x_{i+\frac{1}{2}}\right) \phi_j^{(m_y)}(y) - u\left(t, x_{i-\frac{1}{2}}, y\right) q_1\left(t, x_{i-\frac{1}{2}}, y\right) \phi_i^{(m_x)}\left(x_{i-\frac{1}{2}}\right) \phi_j^{(m_y)}(y) \\ &\quad - \frac{z_x\left(x_{i+\frac{1}{2}}\right)}{2}\left[\left[u\left(t, x_{i+\frac{1}{2}}, y_j\right)\right]\right] \phi_j^{(m_y)}(y) - \frac{z_x\left(x_{i-\frac{1}{2}}\right)}{2}\left[\left[u\left(t, x_{i-\frac{1}{2}}, y_j\right)\right]\right] \phi_j^{(m_y)}(y) dy, \end{aligned} \tag{6.47}$$

where the integrals are expressed by means of the Gauss−Legendre quadrature and

$$\begin{aligned} z_x\left(x_{i+\frac{1}{2}}\right) &= \max\left\{ \left| \mathbf{q}_{1,ij}\left(t, x_{i+\frac{1}{2}}, y_j\right) \phi_i^{(m_x)}\left(x_{i+\frac{1}{2}}\right) \right|, \left| \mathbf{q}_{1,i+1,j}\left(t, x_{i+\frac{1}{2}}, y_j\right) \phi_{i+1}^{(m_x)}\left(x_{i+\frac{1}{2}}\right) \right| \right\}, \\ z_x\left(x_{i-\frac{1}{2}}\right) &= \max\left\{ \left| \mathbf{q}_{1,ij}\left(t, x_{i-\frac{1}{2}}, y_j\right) \phi_i^{(m_x)}\left(x_{i-\frac{1}{2}}\right) \right|, \left| \mathbf{q}_{1,i-1,j}\left(t, x_{i-\frac{1}{2}}, y_j\right) \phi_{i-1}^{(m_x)}\left(x_{i-\frac{1}{2}}\right) \right| \right\}. \end{aligned} \tag{6.48}$$

For the jumps over the element faces, we have

$$\begin{aligned}\left[\left[n\left(t,x_{i-\frac{1}{2}},y\right)\right]\right] &= n_{ij}\left(t,x_{i-\frac{1}{2}},y\right)-n_{i-1,j}\left(t,x_{i-\frac{1}{2}},y\right),\\ \left[\left[n\left(t,x_{i+\frac{1}{2}},y\right)\right]\right] &= n_{i+1,j}\left(t,x_{i+\frac{1}{2}},y\right)-n_{i,j}\left(t,x_{i+\frac{1}{2}},y\right).\end{aligned} \tag{6.49}$$

The y direction is treated analogously. The discretization matrices V_1, V_2, and V_3 are determined similarly to the 1D case. Here Gauss−Legendre quadrature is used per direction. The finally resulting system of ordinary differential equations is integrated over time using the third-order TVD Runge−Kutta method.

6.4.2.3 The Vessels Equation

Reduction of the order of spatial derivatives and using $\mathbf{v}=-\nabla p$ gives

$$\begin{aligned}&\frac{\partial\rho}{\partial t}+D_3\nabla\cdot\mathbf{v}+(\mu_1\mathbf{w}-\chi_2 u\mathbf{q})\cdot\frac{\mathbf{x}}{\|\mathbf{x}\|}+\gamma\left(\rho-\rho_{\text{eq}}\right)=0,\\ &\mathbf{v}+\nabla\rho=0.\end{aligned} \tag{6.50}$$

The weak form simply follows from multiplication by a test function and subsequent integration by parts. Because this equation differs in the 2D case from the 1D case, we give the weak form

$$\begin{aligned}&\int_{e_{ij}}\phi_{ij}\frac{\partial\rho}{\partial t}-D_3\mathbf{v}\cdot\nabla\phi_{ij}+\gamma\phi_{ij}\left(\rho-\rho_{\text{eq}}\right)+\phi_{ij}(\mu_1\mathbf{w}-\chi_2 u\mathbf{q})\cdot\frac{\mathbf{x}}{\|\mathbf{x}\|}d\Omega+\int_{\partial e_{ij}}D_3\phi_{ij}\mathbf{v}\cdot\mathbf{n}d\Gamma=0,\\ &\int_{e_{ij}}\phi_{ij}v_1-\rho\frac{\partial\phi_{ij}}{\partial x}d\Omega+\int_{\partial e_{ij}}\phi_{ij}\rho n_x d\Gamma=0,\\ &\int_{e_{ij}}\phi_{ij}v_2-\rho\frac{\partial\phi_{ij}}{\partial y}d\Omega+\int_{\partial e_{ij}}\phi_{ij}\rho n_y d\Gamma=0.\end{aligned} \tag{6.51}$$

Most of the terms in the above equations are handled using the procedures that we outlined in the earlier subsections. However, for completeness, we present the term with ρ_{eq} and with the snail trail term, that is

$$\begin{aligned}\mathbf{g}_{1ij,m} &= \frac{\Delta x\Delta y}{4}\int_{-1}^{1}\int_{-1}^{1}\gamma\rho_{\text{eq}}P_{m_x}P_{m_y}drds\Rightarrow\mathbf{g}_{1ij}=\frac{\Delta x\Delta y}{4}\gamma\rho_{\text{eq}}\cdot[40\ldots0]^T,\\ \mathbf{g}_{2ij,m} &= \mu_1\frac{\Delta x\Delta y}{4}\sum_{r=1}^{6}\sum_{s=1}^{6}w_r w_s P_{m_x}(x_r)P_{m_y}(y_r)\mathbf{w}(\mathbf{x}_{rs})\cdot\frac{\mathbf{x}_{rs}}{\|\mathbf{x}_{rs}\|},\\ \mathbf{g}_{3ij,m} &= \chi_2\frac{\Delta x\Delta y}{4}\sum_{r=1}^{6}\sum_{s=1}^{6}w_r w_s P_{m_x}(x_r)P_{m_y}(y_r)u(\mathbf{x}_{rs})\mathbf{q}(\mathbf{x}_{rs})\cdot\frac{\mathbf{x}_{rs}}{\|\mathbf{x}_{rs}\|}.\end{aligned} \tag{6.52}$$

Here Gauss−Legendre quadrature has been applied and w_r and w_s are the weights from Table 6.1. Furthermore, the integration points are given by $\mathbf{x}_{rs}=[x_r\ y_s]^T$ where x_r and y_s, respectively, are the weight points in Gauss−Legendre quadrature from Table 6.1. From this, a system of ordinary differential equations is constructed and integrated over time using a third-order TVD Runge−Kutta scheme. The time integration is schematized in Algorithm 6.1.

This algorithm is based on the third-order Runge−Kutta time integration scheme applied on the ordinary differential equations that result after discretizing using the DG equation. The above algorithm entails the one-dimensional case. The two-dimensional case is dealt with analogously, where additional functions are introduced for the vertical coordinate direction.

ALGORITHM 6.1 Time Integration Algorithm

Determine Initial Solution
$n = 0$; $t = 0$
while $t < t_{end}$ **do**
  for $j = 1$ to N **do**
    Compute $\mathbf{c}_j^{(1)}$ using $\mathbf{c}^n$, $\mathbf{q}^n$, $\mathbf{u}^n$, $\mathbf{w}^n$, ρ^n, $\mathbf{v}^n$
    Compute $\mathbf{q}_j^{(1)}$ using $\mathbf{c}_j^{(1)}$
    Compute $\mathbf{u}_j^{(1)}$ using $\mathbf{c}^n$, $\mathbf{q}^n$, $\mathbf{u}^n$, $\mathbf{w}^n$, ρ^n, $\mathbf{v}^n$
    Compute $\mathbf{w}_j^{(1)}$ using $\mathbf{u}_j^{(1)}$
    Compute $\rho_j^{(1)}$ using $\mathbf{c}^n$, $\mathbf{q}^n$, $\mathbf{u}^n$, $\mathbf{w}^n$, ρ^n, $\mathbf{v}^n$
    Compute $\mathbf{v}_j^{(1)}$ using $\rho_j^{(1)}$
    Compute $\mathbf{c}_j^{(2)}$ using $\mathbf{c}^n$, $\mathbf{q}^n$, $\mathbf{u}^n$, $\mathbf{w}^n$, ρ^n, $\mathbf{v}^n$, $\mathbf{c}_j^{(1)}$, $\mathbf{q}_j^{(1)}$, $\mathbf{u}_j^{(1)}$, $\mathbf{w}_j^{(1)}$, $\rho_j^{(1)}$, $\mathbf{v}_j^{(1)}$
    Compute $\mathbf{q}_j^{(2)}$ using $\mathbf{c}_j^{(2)}$
    Compute $\mathbf{u}_j^{(2)}$ using $\mathbf{c}^n$, $\mathbf{q}^n$, $\mathbf{u}^n$, $\mathbf{w}^n$, ρ^n, $\mathbf{v}^n$, $\mathbf{c}_j^{(1)}$, $\mathbf{q}_j^{(1)}$, $\mathbf{u}_j^{(1)}$, $\mathbf{w}_j^{(1)}$, $\rho_j^{(1)}$, $\mathbf{v}_j^{(1)}$
    Compute $\mathbf{w}_j^{(2)}$ using $\mathbf{u}_j^{(2)}$
    Compute $\rho_j^{(2)}$ using $\mathbf{c}^n$, $\mathbf{q}^n$, $\mathbf{u}^n$, $\mathbf{w}^n$, ρ^n, $\mathbf{v}^n$, $\mathbf{c}_j^{(1)}$, $\mathbf{q}_j^{(1)}$, $\mathbf{u}_j^{(1)}$, $\mathbf{w}_j^{(1)}$, $\rho_j^{(1)}$, $\mathbf{v}_j^{(1)}$
    Compute $\mathbf{v}_j^{(2)}$ using $\rho_j^{(2)}$
    Compute $\mathbf{c}_j^{n+1}$ using $\mathbf{c}^n$, $\mathbf{q}^n$, $\mathbf{u}^n$, $\mathbf{w}^n$, ρ^n, $\mathbf{v}^n$, $\mathbf{c}_j^{(2)}$, $\mathbf{q}_j^{(2)}$, $\mathbf{u}_j^{(2)}$, $\mathbf{w}_j^{(2)}$, $\rho_j^{(2)}$, $\mathbf{v}_j^{(2)}$
    Compute $\mathbf{q}_j^{n+1}$ using $\mathbf{c}_j^{n+1}$
    Compute $\mathbf{u}_j^{n+1}$ using $\mathbf{c}^n$, $\mathbf{q}^n$, $\mathbf{u}^n$, $\mathbf{w}^n$, ρ^n, $\mathbf{v}^n$, $\mathbf{c}_j^{(2)}$, $\mathbf{q}_j^{(2)}$, $\mathbf{u}_j^{(2)}$, $\mathbf{w}_j^{(2)}$, $\rho_j^{(2)}$, $\mathbf{v}_j^{(2)}$
    Compute $\mathbf{w}_j^{n+1}$ using $\mathbf{u}_j^{n+1}$
    Compute ρ_j^{n+1} using $\mathbf{c}^n$, $\mathbf{q}^n$, $\mathbf{u}^n$, $\mathbf{w}^n$, ρ^n, $\mathbf{v}^n$, $\mathbf{c}_j^{(2)}$, $\mathbf{q}_j^{(2)}$, $\mathbf{u}_j^{(2)}$, $\mathbf{w}_j^{(2)}$, $\rho_j^{(2)}$, $\mathbf{v}_j^{(2)}$
    Compute $\mathbf{v}_j^{n+1}$ using ρ_j^{n+1}
  end for
  $n \leftarrow n + 1$
  $t \leftarrow t + dt$
end while

6.5 NUMERICAL RESULTS

We present the results after solving Eqs. (6.3)–(6.5). We use the data from Table 6.2.

We consider a hypothetical region that has been effected by fibrosis, where stem cells have been injected. The model assumes that (some of the) stem cells adhere to the fibrotic heart tissue and takes into account a gradual loss over time due to detachment or cellular death. The stem cells secrete chemokines that trigger the endothelial cells to migrate toward the center of the fibrosis inflicted region. This establishes the blood vessel network. First we present some of the one-dimensional results, aiming at illustrating the solutions from the DG method. Subsequently, we present some two-dimensional results.

6.5.1 One-Dimensional Results

In Fig. 6.1, it can be seen that the solution exhibits discontinuities on the element boundaries, which is characteristic for the DG method. At the initial stages, the tip density increases on the boundary of the damage (being located at around $x = 0.1$). Subsequently, the tip density increases as a result of cell proliferation until it reaches a maximum over time. Then the tip density gradually decreases down to zero as time proceeds because the vessel network is gradually forming closed loops, which means that there are no tips anymore. During the same interval, the tips are closing and the vessel density continues to increase so that the damaged part of the heart gets sufficient amounts of oxygen and endothelial cells, which will make the heart tissue less stiff. Next to these results, the error as a function of the grid resolution is plotted in Fig. 6.2. We did this

TABLE 6.2 Input Data in the Simulations

Quantity	Value	Unit
D_1	1	mm^2/s
D_2	0.001	mm^2/s
D_3	0.01	mm^2/s
λ	1	1/s
α	3	$1/(mm^3\ s)$
α_0	50	$1/(mm^3\ mol\ s)$
α_1	10	$1/(mm^3\ mol\ s)$
β_1	0.5	1/s
β_2	50	mm^3/s
χ_1	0.4	$mm^5/(s\ mol)$
χ_2	0.4	$mm^5/(s\ mol)$
γ	0.25	$mm^5/(s\ mol)$
$\hat{c}$	0.2	mol
ρ_{eq}	0.001	$1/mm^3$
m_0	2	–

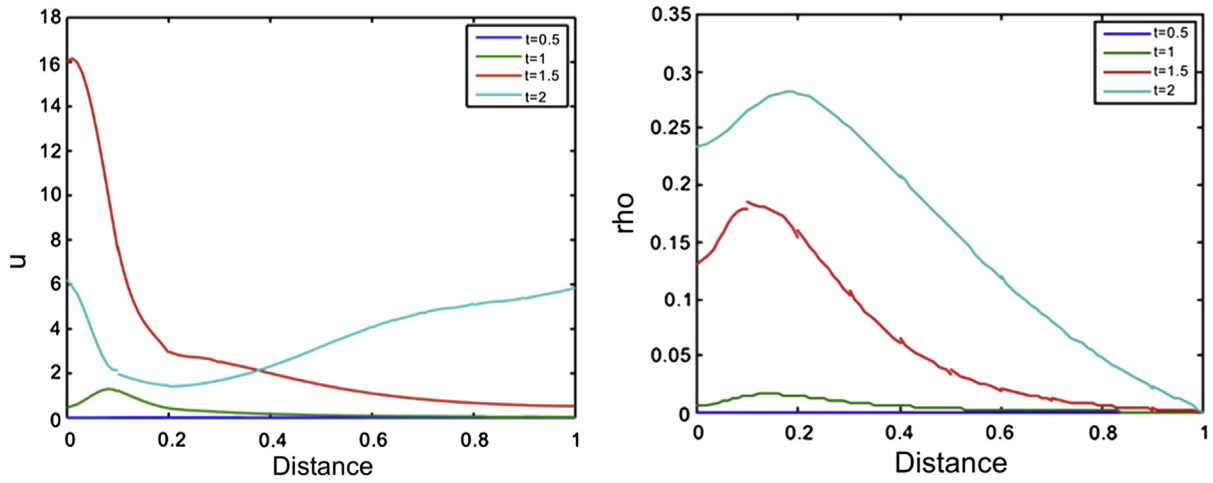

FIGURE 6.1 Top: The tip density u as a function of the distance from the center of the damaged area at various times. Bottom: The vessel density ρ as a function of the distance from the center of the damaged area at various times. The solution was computed using 10 elements and using a DG method with third-order Legendre polynomials $k = 3$ and a time step $\Delta t = 10^{-4}$.

for the advection problem for which we know the exact solution. We determined the order of the method using the L_2-norm, given by

$$\|u_h - u\|^2_{L^2(\Omega)} = \int_\Omega (u_h - u)^2 d\Omega, \tag{6.53}$$

where u_h and u, respectively, represent the DG and exact solution. To compute the norm, Gauss–Legendre quadrature has been used. From the slope in the graph of Fig. 6.2, it follows that $P = 3.9096$, which is only slightly smaller than 4, which is the maximal order of accuracy, given the combination of the time integration and polynomial order of the basis functions.

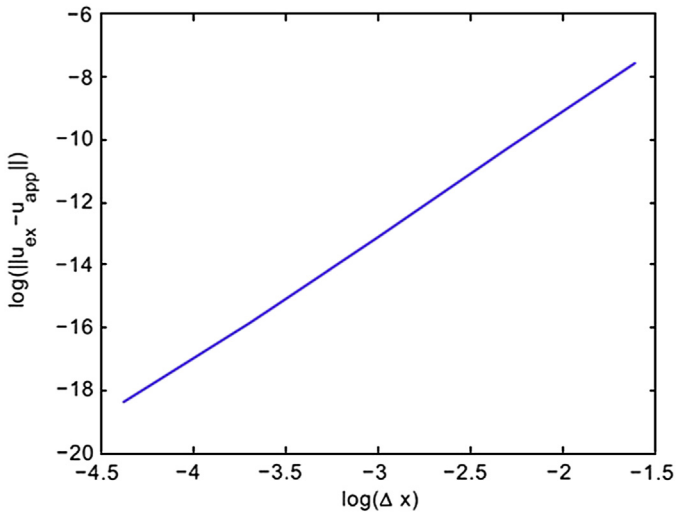

FIGURE 6.2 The error as a function of the element size.

6.5.2 Two-Dimensional Results

Again, we consider the numerical approximation of the solution of Eqs. (6.3)−(6.5) and we use the input data from Table 6.2. For the two-dimensional results, we consider a wound of rectangular geometry. Fig. 6.3 for the tip density shows some interesting minima/maxima. These minima are related to the fact that the wound has a rectangular shape and that the length over which transport from the external boundary takes place changes over the wound edge. Furthermore, after a short time the maxima in the capillary tip density are from the center of the wound to the points of the boundary of the wound on the x- and y-axes. The minima on the wound edge are located on the $y = \pm x$ rays. We see the same phenomenon for the vessel density in Fig. 6.3. From the simulations of Section 6.4.1, we know that the vessel density starts to increase on the boundary of the wound beacuse that is the first location where the attractant vessels and the tips meet. For a rectangular wound this means that the attractant meets vessels and tips at the corner points after meeting of the attractant with the vessels and tips at the other points of the boundary. This occurs due to the fact that the distance from the center to a corner is longer than any other distance from the center to a point on the boundary of the wound. This means that the vessel density on the corner points has increased less than at other points on the boundary after the short time $t = 0.5$. This gives the four minima for the vessel density that are shown in Fig. 6.3. Note that these simulations are done after a relative short

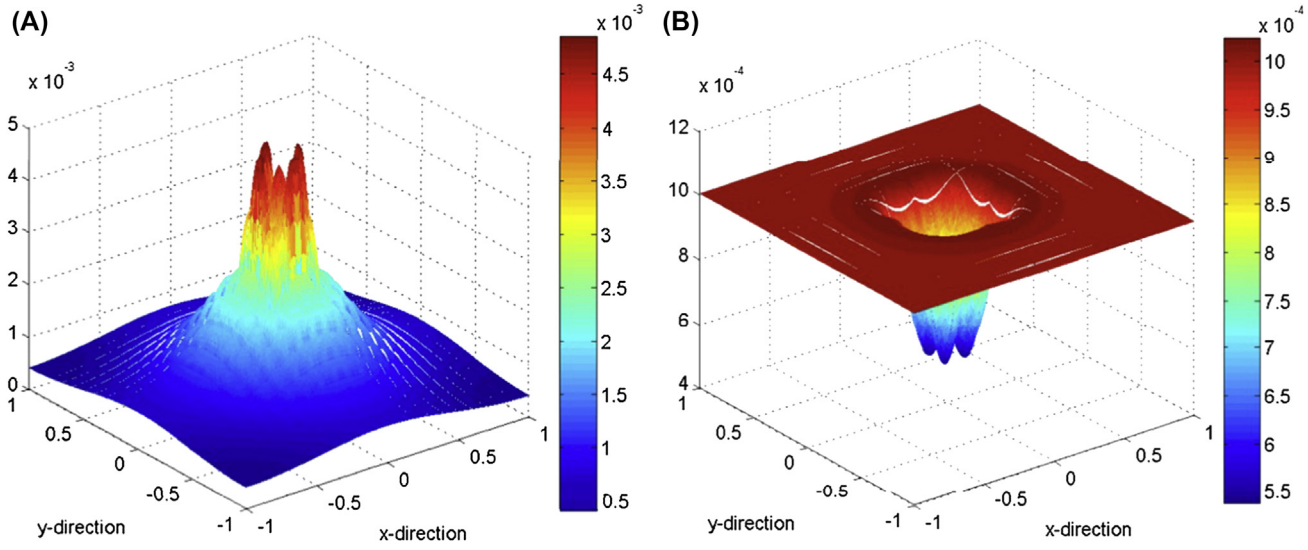

FIGURE 6.3 Three-dimensional snapshot of the tip and vessel density at time $t = 0.5$ with a time step of $\Delta t = 0.0001$.

time $t = 0.5$ so the biological process has just started. Furthermore, we have only used approximations up to order $k = 2$. Because this a relative low order, we have some big discontinuities between the different solutions on the boundaries of the elements. To get better approximations, we should use at least Legendre polynomials up to order $k = 3$.

Certainly, the cost of the method could be improved. At each time we needed to determine the nine coefficients per element (there are 100 elements) corresponding to the nine combinations of polynomials. We needed to do this for all six equations (the concentration TG-β, the capillary tip density, the vessel density, and the three equations caused by the splitting of the diffusion terms). Because we used RK3-TVD for the time integration, we did this calculation three times per time step. Using a time step of $\Delta t = 0.0001$ we did this for all 5000 times to come at $t = 0.5$, which is the time of the simulations plotted in the figures above. In the present computer implementation, one iteration takes approximately 83 s. Therefore, all the 5000 time steps take together approximately 4.83 days. Because this is still just a very short time, we see that it is very expensive. This could be improved by implementing this code in parallel.

6.6 DISCUSSION AND CONCLUSIONS

6.6.1 The Snail Trail Model

First, as mentioned in the model section, the sprouts are assumed to follow the tips. We extended the one-dimensional case in Byrne and Chaplain (1995) to two dimensions where the migration of tips is directed toward the center of the domain of computation, that is, the center of the damaged region. In the present case, this is a reasonable approximation given the symmetry and the damaged region being located around the origin of the domain of computation. However, for more generic cases, the model needs to be revised. In Spill et al. (2015), this issue was treated recently. Because the sprouts follow the location of the tips, the extension of the snail trail is determined by the migration rate of the tips at this location. This needs to be averaged over a representative elementary volume to derive the resulting partial differential equation. Their final result is that the sprout snail trail contribution given by the 1-norm of the flux of tips, that is

$$\frac{\partial \rho}{\partial t} - D_3 \Delta \rho - \left\| D_2 \frac{\partial u}{\partial n} - \chi_1 u \frac{\partial c}{\partial n} \right\|_1 + \gamma\left(\rho - \rho_{\text{eq}}\right) = 0, \quad (t, \mathbf{x}) \in \mathbb{R}^+ \times \Omega, \tag{6.54}$$

or

$$\frac{\partial \rho}{\partial t} - D_3 \Delta \rho - D_2 \left\| \frac{\partial u}{\partial n} \right\|_1 + \chi_1 \left\| u \frac{\partial c}{\partial n} \right\|_1 + \gamma\left(\rho - \rho_{\text{eq}}\right) = 0, \quad (t, \mathbf{x}) \in \mathbb{R}^+ \times \Omega, \tag{6.55}$$

using different assumptions regarding the transition rate between stalk and tip cells. The above 1-norm is taken over the spatial coordinates.

6.6.2 The Numerical Method

To construct a numerical method, which is applicable to the model from Section 6.3 in this chapter, we have to consider different aspects. First, the method should be able to handle complicated geometries because wounds can have any possible shape. Both the finite element method and the DG method are eligible. Because the DG method is more expensive, we first applied the finite element method. This method gave some good results. Secondly, the method should be able to handle hyperbolic or convection-dominated problems. Because if it turns out that the chemotaxis term has more influence than has been assumed, the degree of hyperbolicity of the problem will increase. In the finite element method, the convection term has been made larger by assigning a higher value for the chemotaxis constant χ_1. Unfortunately, we had to conclude from the results that the finite element method was not suitable, unless an ultrahigh grid resolution was used, whereas the DG method was more suitable. Because the DG method meets both requirements, we wanted to implement this method for the two-dimensional model. First we applied the DG method to a relative simple advection equation in one dimension with different kinds of boundary conditions. There, we have introduced a limiter to prevent the appearance of wiggles. In this manuscript, we first described the DG method applied to the one-dimensional model. This is done to present the method and to show some advantages regarding accuracy of this method in comparison to the finite element method. Subsequently, we used it to construct the approximations to the two-dimensional model. The DG method was found to be a very complex and expensive method. Therefore, we were only able to approximate situations with a two-dimensional circular wound (using polar coordinates, see Crapts, 2012) and situations with a rectangular-shaped wound using rectangular elements.

The DG method is relatively expensive due to several facts. First, the DG method has many degrees of freedom which makes the method very expensive. Think of N, the number of elements and $p + 1$ the number of basis functions per

element. The higher the order of the Legendre Polynomials, the more accurate the approximation is; however, also the more the degrees of freedom, the more expensive the method. Secondly, we used the so-called local DG method, which is an extension of the DG method with Runga−Kutta time integration for purely hyperbolic or convection-diffusion systems. This results into the high-order accuracy and easy handling of complicated geometries. Basically, it means splitting the diffusion term such that we obtain a second equation for each equation of our model. The more equations to solve, the more expensive the method becomes. Finally, we use the central flux, which uses a stencil of five elements, instead of an upwind or downwind flux, which uses a stencil of only three elements. We do this because the central flux is the only one that gives good results. The disadvantage is again that it is more expensive. However, we note that the DG method can achieve a given error tolerance faster than a low-order method. In addition, the flux can be improved by performing suitable stability analysis for this equation.

Our DG method can handle the complicated geometries and the relative high degree of hyperbolicity of the model. The only problem is that the method is very expensive; hence the question whether the DG method is suitable to use for application is quite legitimate. The long computation times make the method unattractive at the moment. Hence the method could be improved by implementing in parallel or suitable use of graphics processing unit (GPU) computers.

In the framework of a literary study, we tried to improve the finite element approximations for the convection dominated problem, in only one dimension. At that moment only basic SUPG method was implemented and it did not improve the simulations. Because we only implemented some basic SUPG, we cannot exclude SUPG as one of the options to improve the approximations. Therefore, for further research, the option to improve the approximations using the finite element with SUPG should be reconsidered.

We performed some simulations using the DG method for our model with a square-shaped wound. Because of limited computational resources, we were only able to perform the simulations to time $t = 0.5$, when the biological process has just begun. In these simulations we already see some differences with respect to the simulations for a circular wound. To draw more and better conclusions about the healing of a square wound, the simulation should run for a longer time. Furthermore, we have only used Legendre polynomials up to order 2. To get a better approximation, we need at least an approximation that uses Legendre polynomials up to order 3. To be able to say more about the healing of a rectangularly shaped wound, the simulation should run for a rectangular wound because we have only done it for a square wound. The same Matlab code can be used for this. While determining the approximations to the solution of the equations in the model, in one and two dimensions, using the DG method, we did not use a limiter of any kind. It was not necessary because no wiggles appeared. However, it is worth investigating whether a limiter may improve the approximation. Note that the use of a limiter would add additional expense.

We also remark that this is, as far as we know, the first simulation study on stem cell treatment in the framework of postcardiac infarction treatment. At this stage, experimental validation is beyond the scope of the manuscript. This manuscript should be considered as a feasibility study where it is illustrated that the DG method can be applied to the modeling of this class of biomedical phenomena.

REFERENCES

Atkinson, K., Han, W., 2009. Theoretical Numerical Analysis, third ed. Springer, Dordrecht, Heidelberg, London, New York.

Baek, S.J., Kang, S.K., Ra, J.C., 2011. In vitro migration capacity of human adipose tissue-derived mesenchymal stem cells reflects their expression of receptors for chemokines and growth factors. Experimental and Molecular Medicine 43, 596−603.

Bookholt, F.D., Monsuur, H.N., Gibbs, S., Vermolen, F.J., 2016. Mathematical modelling of angiogenesis using continuous cell-based models. Biomechanics and Modelling in Mechanobiology 15 (6), 1577−1600.

Brenner, S.C., Scott, L.R., 2008. The Mathematical Theory of Finite Element Methods, third ed. Springer.

Byrne, H.M., Chaplain, M.A.J., 1995. Explicit Solutions of a Simplified Model of Capillary Sprout Growth During Tumor Angiogenesis. School of Mathematical Sciences, University of Bath, Claverton Down, Bath BA2 7AY, UK.

Cockburn, B., 1997. An introduction to the discontinuous Galerkin method for convection-dominated problems. In: Quarteroni, A. (Ed.), Advanced Numerical Approximation of Nonlinear Hyperbolic Equations (Lecture Notes in Mathematics).

Crapts, L.Y.D., 2012. Modelling an Angiogenesis Treatment After a Myocardial Infarction. M.Sc. thesis at the Delft Institute of Applied Mathematics. Delft University of Technology, The Netherlands. Downloadable at: http://repository.tudelft.nl.

Epshteyn, Y., Izmirlioglu, A., 2009. Fully discrete analysis of a discontinuous finite element method for the Keller-Segel chemotaxis model. Journal of Scientific Computing 40, 211−256.

Epshteyn, Y., Kurgonov, A., 2008. New interior penalty discontinuous Galerkin methods for the Keller-Segel chemotaxis model. SIAM Journal on Numerical Analysis 47, 386−408.

Epshteyn, Y., 2009. Discontinuous Galerkin methods for the chemotaxis and haptotaxis models. Journal of Computational and Applied Mathematics 244 (1), 168−181.

Epshteyn, Y., 2012. Upwind-difference potentials method for Patlak-Keller-Segel chemotaxis model. Journal of Scientific Computing 53, 689−713.
Fomovsky, G.M., Holmes, J.W., 2010. Evolution of scar structure, mechanics, and ventricular function after myocardial infarction in the rat. Americal Journal of Physiology. Heart and Circulation Physiology 298 (1), H221−H228.
Gottlieb, S., Shu, C.-W., 1998. Total variation diminishing Runge-Kutta schemes. Mathematics of Computation 67, 73−85.
Hesthaven, J.S., Warburton, T., 2008. Nodal Discontinuous Galerkin Methods. Springer, New York.
Kajstura, J., Hosoda, T., Bearzi, C., Rota, M., Maestroni, S., Urbanek, K., Leri, A., Anversa, P., 2008. The human heart: a self-renewing organ. Clinical and Translational Science 1 (1), 80−86.
Lazzerini, P.E., Capecchi, P.L., Guideri, F., Acampa, M., Galeazzi, M., Laghi Pasini, F., 2006. Connective tissue diseases and cardiac rhythm disorders: an overview. Autoimmunity Reviews 5 (5), 306−313.
Leveque, R.J., 2002. Finite Methods for Hyperbolic Problems. Cambridge Texts in Applied Mathematics, sixth ed. Cambridge University Press, New York.
Maggelakis, S.A., 2003. A mathematical model of tissue replacement during epidermal wound healing. Applied Mathematical Modelling 27, 189−196.
Maggelakis, S.A., 2004. Modeling the role of angiogenesis in epidermal wound healing. Discrete and Continuous Dynamical Systems − Series B 4 (1), 267−273.
Mirzaee, H., Ryan, J.K., Kirby, R.M., 2014. Smoothness-increasing accuracy-conserving (SIAC) filters for discontinuous Galerkin solutions: application to structured tetrahedral meshes. Journal of Scientific Computing 58, 690−704.
Moller, M., 2013. Algebraic flux correction for nonconforming finite element discretizations of scalar transport. Computing 95 (5), 425−448.
Oers, R.F.M., Rens, E.G., LaValley, D.J., Reinhart−King, C.A., Merks, R.M.H., 2014. Mechanical cell−matrix feedback explains pairwise and collective endothelial cell behavior in vitro. PLoS Computational Biology 10 (3), e1003774.
Olivetti, G., Melissari, M., Capasso, J.M., Anversa, P., 1991. Cardiomyopathy of the aging human heart. Myocyte loss and reactive cellular hypertrophy. Circulation Research 68 (6), 1560−1568.
Paillere, H., 1996. Multidimensional upwind residual distribution schemes for the convection-diffusion equation. International Journal for Numerical Methods in Fluids 23 (9), 923−936.
Pettet, G.J., Byrne, H.M., McElwain, J., Norbury, J., 1996. A model of wound-healing angiogenesis in soft tissue. Mathematical Biosciences 136 (1), 35−63.
Przybyt, E., Harmsen, M.C., 2013. Mesenchymal stem cells: promising for myocardial regeneration? Current Stem Cell Research and Therapy 8 (4), 270−277.
Qiu, J., Shu, C.-W., 2005. Runge−Kutta discontinuous Galerkin method using Weno limiters. SIAM Journal of Scientific Computing 26 (3), 907−929.
Shimamoto, T., 1969. Experimental study on atherosclerosis − an attempt at its prevention and treatment. Acta Pathologica Japanonica 19 (1), 15−43.
Spill, F., Guerrero, P., Alarcon, T., Maini, P.K., Byrne, H.M., 2015. Mesoscopic and continuum modelling of angiogenesis. Journal of Mathematical Biology 70 (3), 485−532.
Talman, V., Ruskoaho, H., 2016. Cardiac fibrosis in myocardial infarction − from repair and remodelling to regeneration. Cell and Tissue Research 365 (3), 563−581.
Wingstrand, V.L., Larsen, C.G., Jensen, D.H., Bork, K., Sebbesen, L., Balle, J., von Buchwald, C., 2016. Mesenchymal stem cell therapy for the treatment of vocal fold scarring: a systematic review of preclinical studies. PLoS One 11 (9), e0162349.

FURTHER READING

Flegg, J.A., Byrne, H.M., McElwain, D.L.S., 2010. Mathematical model of hyperbaric oxygen therapy applied to chronic diabetic wounds. Bulletin of Mathematical Biology 72, 1867−1891.